Marine and biomass burning aerosols in the southern Indian Ocean: Retrieval of aerosol optical properties from shipborne lidar and Sun photometer measurements

Valentin Duflot, P. Royer, P. Chazette, Jean-Luc Baray, Yann Courcoux, Robert Delmas

Marine and biomass burning aerosols in the southern Indian Ocean: Retrieval of aerosol optical properties from shipborne lidar and Sun photometer measurements

V. Duflot,[1] P. Royer,[2,3] P. Chazette,[2] J.-L. Baray,[1] Y. Courcoux,[1] and R. Delmas[1]

Received 23 February 2011; revised 31 May 2011; accepted 29 June 2011; published 27 September 2011.

[1] We document aerosol extinction properties in the southern Indian Ocean. A unique data set of shipborne measurements has been collected with a dual Rayleigh-Mie lidar aboard the research vessel Marion Dufresne during two campaigns: one around Madagascar during the Southern Hemisphere late summer and one close to the Kerguelen Islands during the biomass burning (BB) season. During this latter, a layer containing a mix of BB and marine aerosols extending up to ~3 km above mean sea level (amsl) has been observed from [31°S, 69°E] to [24°S, 59°E]. Both vertical structure and aerosol optical properties have been retrieved from the inversion of the lidar signals. Sun photometer-derived aerosol optical thickness (AOT) at 355 nm is used to constrain the lidar inversion. We obtain a mean integrated value of backscatter-to-extinction ratio (BER) (extinction-to-backscatter ratio, or so-called lidar ratio, LR) of 0.039 ± 0.009 sr^{-1} (26 ± 6 sr) and 0.021 ± 0.006 sr^{-1} (48 ± 12 sr) for the marine aerosols layer, and for the mixing between BB and marine aerosols with an uncertainty of 0.009 sr^{-1} (6 sr) and 0.004 sr^{-1} (9 sr), respectively. Lidar calibration is used to inverse data without any simultaneous Sun photometer measurements (as nighttime data), and the temporal evolution of the optical properties and vertical extension of the BB aerosol plume is documented. The presence of BB aerosols is in agreement with Lagrangian model GIRAFE v3 (reGIonal ReAl time Fire plumEs) simulations, which show the South American and Southern African BB origin of the encountered aerosol layer.

Citation: Duflot, V., P. Royer, P. Chazette, J.-L. Baray, Y. Courcoux, and R. Delmas (2011), Marine and biomass burning aerosols in the southern Indian Ocean: Retrieval of aerosol optical properties from shipborne lidar and Sun photometer measurements, *J. Geophys. Res.*, *116*, D18208, doi:10.1029/2011JD015839.

1. Introduction

[2] Aerosols are efficient scatters of solar radiation. Consequently, they often have a large impact on local and regional visibility, contribute to the planetary albedo and affect regional and global climate [*Crutzen and Andreae*, 1990; *Andreae*, 1996]. Spatially and temporally resolved information on the atmospheric burden and radiative properties of aerosol is needed to estimate radiative forcing [*Intergovernmental Panel on Climate Change*, 2007]. Moreover, many of the pyrogenic particles can act as cloud condensation nuclei (CCN) [*Rogers et al.*, 1991] and thereby change the radiative properties of clouds. Local fossil fuel and agricultural biomass burning (BB) cause a high aerosol loading over the Indian Ocean [*Lelieveld et al.*, 2001]. Aerosol loading and extinction properties have been intensely studied over the region of the northern Indian Ocean and Arabian sea in the framework of the INDian Ocean EXperiment (INDOEX) during the winter monsoon [*Rajeev et al.*, 2000; *Léon et al.*, 2001; *Pelon et al.*, 2002; *Ramanathan et al.*, 2001; *Rasch et al.*, 2001; *Welton et al.*, 2002; *Chazette*, 2003; *Forêt et al.*, 2006].

[3] However, compared to the Northern Hemisphere and to the northern Indian Ocean, the southern Indian Ocean is quite an aerosol-clean area, except during the Southern Hemisphere BB season. The Southern African Regional Science Initiative (SAFARI 2000) experiment showed pronounced smoke and haze exiting off the South-Southeast Africa during the Southern Hemisphere BB season going from July to October. Such plumes are advected over southern Indian Ocean [*Annegarn et al.*, 2002] and can attain Australia [*Rosen et al.*, 2000] and New Zealand [*Edwards et al.*, 2006]. Long-range transports of BB pollution can also occur from South America and Southeast Asia into the southern Indian Ocean during the Southern Hemisphere BB season [*Edwards et al.*, 2006; *Duflot et al.*, 2010]. The resulting aerosol loading causes an increase of the aerosol optical thickness (AOT_λ) and modifies the extinction properties of the low troposphere. Since this seasonal variation of the tropospheric aerosol loading in the southern Indian Ocean

[1]Laboratoire de l'Atmosphère et des Cyclones, Université de la Réunion, UMR CNRS-Météo-France 8105, Saint-Denis, Réunion, France.
[2]Laboratoire des Sciences du Climat et de l'Environnement, UMR CEA-CNRS-UVSQ 8212, Gif-sur-Yvette, France.
[3]LEOSPHERE, Paris, France..

0148-0227/11/2011JD015839

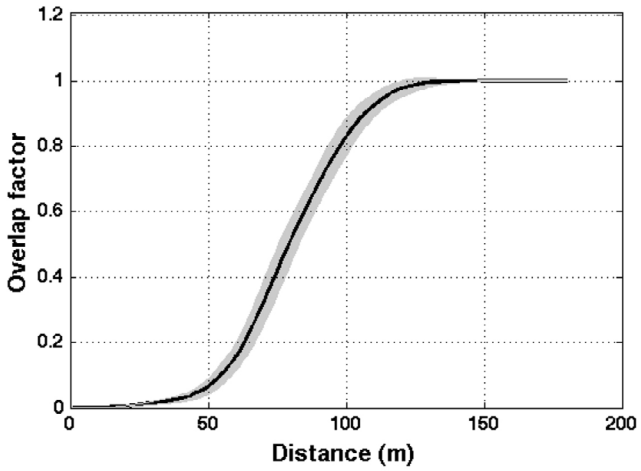

Figure 1. Lidar mean overlap factor F (black solid line) and its standard deviation (gray shaded area) as a function of the distance from the laser source.

is due to agricultural needs and cultural habits, it occurs every year, and should last still for a long time.

[4] Due to few ground-based measurement points, only big scale means such as MODerate-resolution Imaging Spectroradiometer (MODIS) onboard Terra and Aqua platforms and the Cloud-Aerosol Lidar with Orthogonal Polarization (CALIOP) lidar onboard Cloud-Aerosol Lidar and Infrared Pathfinder Satellite Observation (CALIPSO) are available to study the BB aerosol optical properties over the southern Indian Ocean. However, the effect of aerosols on climate strongly depends on their optical properties and tridimensional distribution, and these parameters cannot be easily retrieved from spaceborne instruments, mainly in presence of low AOT, which is often associated with measurements performed with a small signal-to-noise ratio. Ground-based lidars offer the opportunity to measure simultaneously the vertical structure and the extinction coefficient of the atmospheric aerosol layers with a high vertical and temporal resolution, and are complementary to satellite observations.

[5] The data presented here give detailed information on the vertical distribution and optical properties over southern Indian Ocean's marine and BB aerosols. These data have been acquired during two ship-based experiments: one around Madagascar in late austral summer 2009 and another one between La Réunion (21°S, 55°E) and the Kerguelen Islands (50°S, 70°E) in austral winter 2009 during the Southern Hemisphere BB season. In Section 2 the experimental set up involved in this experiment is detailed. The method and the results are presented in Section 3 and discussed in Section 4 taking into account uncertainties on retrievals.

2. Data and Numerical Tools

2.1. Experimental Set Up and Networks

2.1.1. Rayleigh-Mie Lidar

[6] The Rayleigh-Mie lidar used is a LEOSPHERE ALS450® based on a Nd:Yag laser producing pulses with a mean energy of 16 mJ at 355 nm and a frequency of 20 Hz. The system was installed in an air-conditioned box adapted for use in severe conditions. Lidar measurements have been averaged over 2 min with a vertical resolution of 15 m. The lidar profiles enable to retrieve aerosol optical properties (extinction and backscatter coefficient in synergy with Sun photometer measurements) and atmospheric structures (boundary layer heights, aerosol layers and clouds). It is particularly well-adapted to open ocean experiment and MBL study thanks to its full-overlap height reached at ~120 m (Figure 1). The overlap factor (F) has been retrieved using horizontal laser shots both before and after the campaigns as described by *Chazette* [2003] assuming the atmosphere stable horizontally.

2.1.2. Sun Photometer, AERONET, and Maritime AERONET

[7] AOT measurements were performed in clear-sky condition using a MICROTOPS II Sun photometer instrument (Solar Light, Inc.). The instrument field of view is about 1°. The AOT (AOT_λ) is measured at five wavelengths (λ) in the visible spectrum (380, 500, 675, 870 and 1020 nm). The measurements realized with the Sun photometer during the two campaigns are part of the Maritime Aerosol Network (MAN) data. MAN is a component of the Aerosol Robotic Network (AERONET), affiliated with the AERONET calibration and data processing, and deploys ship-based handheld Sun photometers to complement measurements where no islands exist [*Smirnov et al.*, 2009]. The instrument was calibrated at the NASA Goddard Space Flight Center against the AERONET reference CIMEL Sun/sky radiometer. The data presented here have been quality- and cloud-screened following the methodology of *Smirnov et al.* [2000] and the mean uncertainty on the AOT measurements equals 0.015 [*Pietras et al.*, 2002]. The AOT at the lidar wavelength of 355 nm (AOT_{355}) was calculated from AOT_{380} using the Ångström exponent [*Ångström*, 1964] between 380 and 500 nm. The uncertainty on the retrieved AOT_{355} has been computed following a similar approach showed by *Hamonou et al.* [1999].

2.1.3. MODIS

[8] The MODIS instrument onboard the Terra and Aqua satellites (http://modis.gsfc.nasa.gov/) enables active fire detection based on the high infrared emissions of the fires [*Giglio et al.*, 2003]. This information is available via the FIRMS site (Fire Information for Resource Management System) developed by the University of Maryland (http://maps.geog.umd.edu/firms/). FIRMS delivers active fires spots using the MODIS active fire locations processed by the MODIS Rapid Response System using the standard MODIS MOD14 Fire and Thermal Anomalies Product. Each active fire location represents the center of a 1 km pixel that is flagged by the algorithm as containing a fire within the pixel.

[9] We also have used AOT_{500} as retrieved by MODIS on board the Terra spacecraft with a 10 × 10 km^2 horizontal resolution (at nadir, level 3 data). The retrieval of aerosol properties over both land [*Kaufman et al.*, 1997] and ocean [*Tanré et al.*, 1997] makes use of seven spectral channels in the solar spectrum (0.47–2.1 mm).

2.1.4. Ship Plan

[10] Lidar and Sun photometer measurements were performed aboard the French research vessel Marion Dufresne around Madagascar from 19 April to 13 May, 2009, during the so-called Measurement of Aerosols in the Mozambique

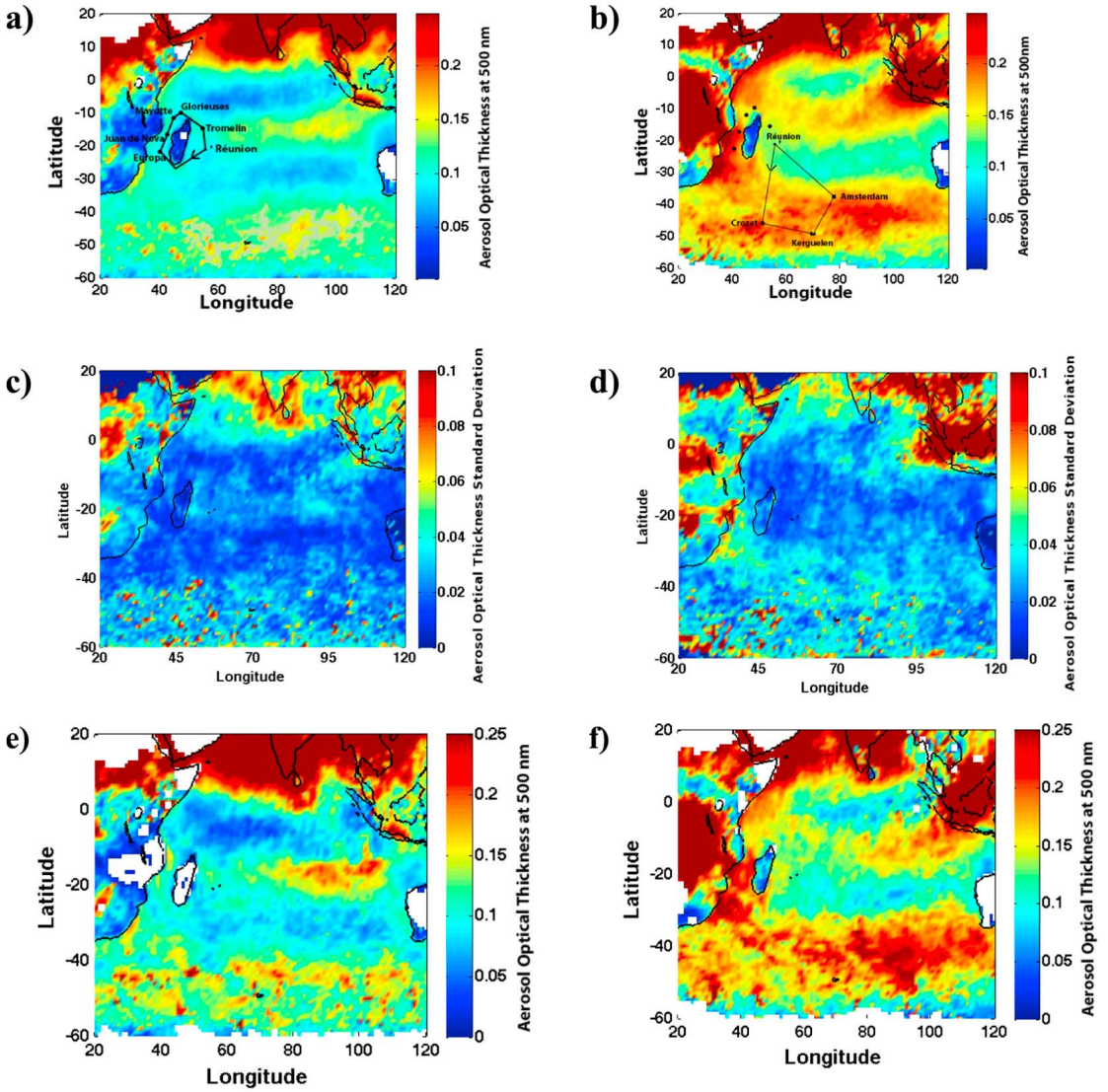

Figure 2. (a) Monthly mean AOT_{500} retrieved from MODIS for the month of April over the years 2002 to 2009 and track of the research vessel Marion Dufresne around Madagascar in April–May 2009. (b) Monthly mean AOT_{500} retrieved from MODIS for the month of September over the years 2002 to 2009 and track of the research vessel Marion Dufresne in August–September 2009. (c) Standard deviation of the monthly mean AOT_{500} retrieved from MODIS for the month of April over the years 2002 to 2009. (d) Standard deviation of the monthly mean AOT_{500} retrieved from MODIS for the month of September over the years 2002 to 2009. (e) Monthly mean AOT_{500} retrieved from MODIS for the month of April 2009. (f) Monthly mean AOT_{500} retrieved from MODIS for the month of September 2009.

Channel (MACAMOZ) campaign, and from La Réunion (21°S, 55°E) to Kerguelen Islands (50°S, 70°E) from 21 August to 17 September, 2009, during the so-called Kerguelen Aerosols Measurement from African Sources and plUmes Trajectory Reverse Analysis (KAMASUTRA) campaign. Figures 2a and 2b show the tracks of the two campaigns superimposed on the mean AOT at 500 nm retrieved over Indian Ocean from MODIS Aqua in April (Figure 2a) and September (Figure 2b) from 2002 to 2009. Such information gives climatology of the aerosol loading in the area for the two periods. One can see that the aerosol loading in April (Figure 2a) around Madagascar is low ($AOT_{500} < 0.1$): this is not the Southern Hemisphere BB season and the free troposphere is quite clean of aerosol. The main contribution in the central Indian Ocean is due to emissions from the Indian subcontinent and Southeast Asia with a mean $AOT_{500} \sim 0.15 \pm 0.04$.

[11] A more important aerosol loading is noticed between La Réunion and Kerguelen Islands in September (Figure 2b) characterized by higher mean $AOT_{500} \sim 0.2$ and a larger footprint on the southern part of the Indian Ocean. Note that the contribution of Indonesia is enhanced compared with the previous period. The two plumes are mainly due to the contributions of biomass burning that occur during this season. One can notice the stream of air masses loaded in BB smoke exiting off the South-Southeast Africa toward

south Australia [*Annegarn et al.*, 2002] and the one going from Indonesia-Malaysia to the La Réunion area during the Southern Hemisphere BB season [*Duflot et al.*, 2010].

[12] Figures 2c and 2d show the standard deviation of the monthly mean AOT_{500} over the years 2002–2009: this gives the temporal variability of the aerosol loading patterns from one year to another for the two periods. The standard deviation of AOT_{500} along the MACAMOZ campaign's track (Figure 2c) is low (<0.03), which suggests that the low aerosol loading in this area in April is quite constant from one year to another. Figure 2e shows that the situation is quite similar to the climatological pattern for April 2009. The standard deviation of AOT_{500} along the KAMASUTRA campaign's track (Figure 2d) is below 0.05; as the mean AOT_{500} in the plume exiting off the South-Southeast Africa toward the Southwestern Indian Ocean is larger than 0.15 and can reach 0.3 in the plume center, this suggests that this plume is present every year in September. Figure 2e shows that the situation is very close to the climatological pattern for September 2009.

[13] Consequently, the MACAMOZ campaign around Madagascar in April 2009 was focused on testing the instrumental set up and on retrieving the optical properties of the marine aerosols trapped in the marine boundary layer (MBL) while the KAMASUTRA campaign between La Réunion and Kerguelen Islands in September 2009, taking place during the Southern Hemisphere BB season, was focused on retrieving the optical properties of the BB aerosols.

2.2. GIRAFE-FLEXPART

[14] The GIRAFE (reGIonal ReAl time Fire plumEs) v3 model combines the MODIS fire counts system with the FLEXPART 6.2 Lagrangian model: at each fire pixel location detected by MODIS, a number of numerical particles is emitted and advected by the FLEXPART 6.2 code. The 0.5 × 0.5 gridded fire-counts are corrected for spatial variability in the frequency of satellite overpasses and missing observations. FLEXPART version 6.2 is a Lagrangian particle dispersion model [*Stohl et al.*, 2005], which simulates the transport and dispersion of linear tracers and treats advection and turbulent diffusion by processing the trajectories of a multitude of particles. The FLEXPART model was driven by global wind field data from ECMWF, with a horizontal resolution of 1 × 1 degree and 60 vertical levels, and a temporal resolution of 4 h. During the measurement campaign, daily GIRAFE simulations over 5 days in forecast mode were performed in order to anticipate the crossing of a BB plume. The particles were injected above fire pixels for 6 h. As recommended by *Dentener et al.* [2006], particles were emitted up to 2000 m agl (above ground level) for each fire pixel detected by MODIS.

3. Data Analysis

[15] In this section, the lidar calibration is first explained (Section 3.1). We then present the method used to inverse the lidar signal using the AOT simultaneously measured by Sun photometer (Section 3.2). Only marine aerosols were encountered during the MACAMOZ campaign around Madagascar during the early winter season. We thus use the acquired data to characterize the MBL and the optical properties (i.e., the vertical profile of aerosol extinction coefficient and the representative backscatter-to-extinction ratio BER_λ at the wavelength λ, as well as the lidar ratio LR_λ – which is the inverse of the BER_λ) of the marine aerosols in this part of the Indian Ocean (Section 3.2.1). A BB aerosol layer was encountered during the KAMASUTRA campaign toward Kerguelen Islands during the Southern Hemisphere BB season. We use the AOT simultaneously measured by Sun photometer to characterize the vertical expansion of the BB aerosol loaded layer, as well as its optical properties (Section 3.2.2.1). In Section 3.2.2.2, we use the instrumental constant computed in Section 3.1 to inverse nighttime lidar profiles (and other times without Sun photometer) and to access the evolution with time of the aerosols optical properties and extinction profiles during the crossing of the encountered BB aerosol plume.

3.1. Lidar Calibration

[16] After correction of the sky radiance, the lidar equation gives the range-corrected signal $S(z)$ for the emitted wavelength of λ = 355 nm as a function of the range z, the total (molecular and aerosol) backscatter $\beta_{355}(z)$ and extinction coefficients $\alpha_{355}(z)$ [*Measures*, 1984]:

$$S(z) = \frac{C_\lambda}{(z_0 - z)^2} . F(z) . \beta_{355}(z) . \exp\left(-\frac{2}{\cos\theta} . \int_{z_0}^{z} \alpha_{355}(z') \cdot dz' \right) \quad (1)$$

where θ is the pointing angle, C_λ is a constant which characterizes the overall efficiency of the lidar system implemented at the altitude z_0 and $F(z)$ is the overlap factor (see Figure 1). In analog mode the instrumental constant is a function of optical efficiency, reception area, laser energy, amplification and photomultiplier gain.

[17] In order to calibrate the lidar (i.e., compute the instrumental constant C_λ), we used simultaneously (5 min around the lidar acquisition time) Sun photometer-derived AOT_{355}. In clear sky condition, above the aerosol layers where only molecular scattering occurs at the altitude z_m, the lidar equation becomes for a vertically pointing lidar:

$$S(z_m) = \frac{C_\lambda}{(z_0 - z)^2} \beta^m_{355}(z_m) \cdot \exp\left[-2 \left(\underbrace{\tau^a_{355}(z_0, z_m)}_{AOT_{355}} + \tau^m_{355}(z_0, z_m) \right) \right] \quad (2)$$

where $\beta^m_{355}(z_m)$ is the molecular backscatter and $\tau^m(z_0, z_m)$ the optical thickness at 355 nm between z_0 and z_m which are determined from climatological radiosounding profiles (pressure, temperature) using the polynomial approximation proposed by *Nicolet* [1984].

[18] Then, C_λ is given against the Sun photometer measurements by:

$$C_\lambda = \frac{(z_0 - z)^2}{\beta^m_{355}(z_m)} S(z_m) \cdot \exp\left[2 \left(AOT_{355} + \tau^m_{355}(z_0, z_m) \right) \right] \quad (3)$$

Figure 3a shows the mean vertical profile of the apparent backscatter coefficient derived from the lidar signals used for the calibration superimposed on the simulated pure molecular backscatter coefficient. The altitude reference at which only molecular scattering occurs was taken between 3 and 4 km.

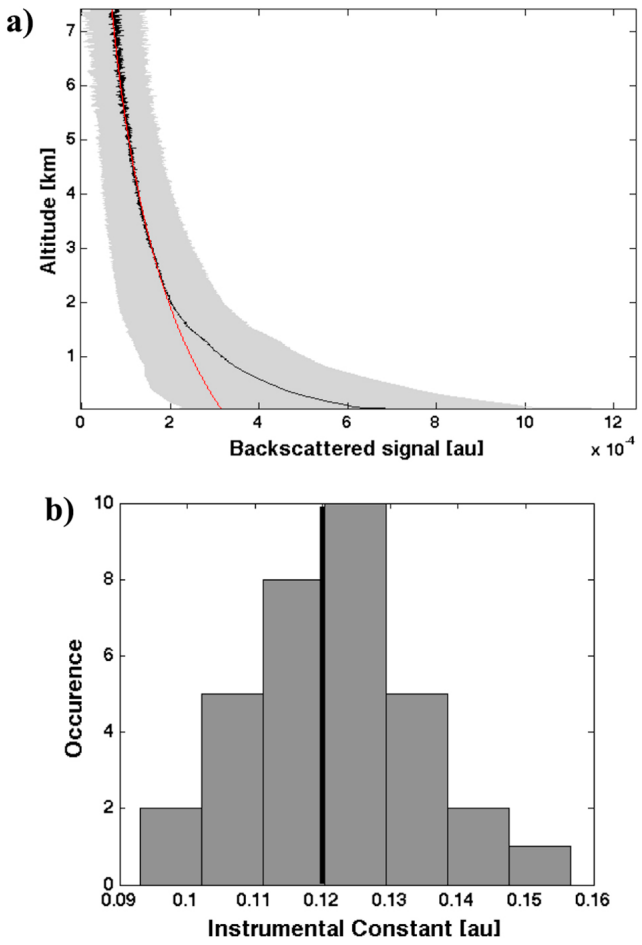

Figure 3. (a) Mean (black line) and standard deviation (gray area) of the vertical profile of the apparent backscatter coefficient used for the lidar calibration. The red line shows the simulated pure molecular scattering signal used for the calibration. (b) Histogram of the retrieved C_λ. The mean C_λ (0.12 [au]) is given by the black vertical bar.

[19] Figure 3b shows the histogram of the retrieved C_λ. The mean C_λ is 0.12 [au] with a standard deviation of 0.014 [au]. The mean C_λ will be used in Section 3.2.2.2 to inverse lidar signals without any simultaneous Sun photometer measurements.

3.2. Lidar-Derived Aerosol Optical Properties

[20] In this section, Sun photometer measurements are used to constrain the lidar inversion [*Chazette*, 2003]. The backscatter lidar equation is underdetermined due to its dependence on two unknowns: aerosol backscatter (or extinction) coefficient and BER_{355} [*Klett*, 1985; *Chazette*, 2003]:

$$\beta^m_{355}(z) = \frac{(z-z_0)^2 \cdot S(z) \cdot Q(z)}{(z_r-z_0)^2 \cdot \frac{S(z_r)}{\beta^m_{355}(z_r)} + \frac{2}{BER_{355}} \cdot \int_z^{z_r} (z'-z_0)^2 \cdot S(z') \cdot Q(z') \cdot dz'}$$

$$\text{with } Q(z) = \exp\left[2 \cdot \left(\frac{3}{8\pi \cdot BER_{355}} - 1\right) \cdot \int_z^{z_r} \alpha^m_{355}(z') \cdot dz'\right] \quad (4)$$

where z_r is the reference altitude corresponding to the integration constant of the Bernouilli differential equation.

[21] Hence, lidar data are inverted to retrieve both the vertical profile of the aerosol extinction coefficient and BER_{355} using the Bernoulli's differential form of the propagation equation [*Klett*, 1985] and a dichotomous approach where BER_{355} is increased (decreased) if the lidar-derived optical thickness is larger (lower) than the Sun photometer-derived AOT_{355} simultaneously acquired. The dichotomous approach is stopped when the difference between estimated and calculated optical thickness becomes less than the error on AOT_{355}. It is noteworthy that this method gives access to a height-independent BER_{355} value.

[22] Hereafter, we investigate the data acquired during the MACAMOZ and KAMASUTRA campaigns to document the optical properties of the marine and BB aerosols. We used two criteria to discriminate the cases containing only marine aerosols from the cases containing marine and another type of aerosols: 1) the shape of each lidar range-corrected signal (corrected from the sky background and the solid angle) is compared to the shape of a simulated signal assuming only Rayleigh backscattering; 2) the simultaneously (5 min around the lidar acquisition time) acquired Sun photometer-derived AOT_{355} is compared to a threshold equal to 0.10. If the Sun photometer-derived AOT_{355} is below this threshold and if the shape of the simultaneously acquired lidar signal matches the shape of the pure Rayleigh simulated signal except in the MBL (supposed to be less than 1 km thick), then the case is classified as containing only marine aerosols. Using this approach, it appears that no BB aerosols events have been detected during the MACAMOZ campaign, and that a BB aerosols plume was crossed during the KAMASUTRA campaign. Thus, we use the data acquired during the MACAMOZ campaign to document only the optical properties of the marine aerosols (Section 3.2.1), and we use the data acquired during the KAMASUTRA campaign to document the optical properties of the BB and marine aerosols (Section 3.2.2).

3.2.1. MACAMOZ Campaign: Optical Properties of the Marine Aerosols

[23] Figure 4 (top left) shows the synthesis of the Sun photometer measurements during the whole MACAMOZ campaign. We use two independent variables: AOT_{380} and Ångström exponent (a) between 500 and 675 nm. Mean AOT_{380} is 0.08 and mean a is 0.63. One can notice that all AOT_{380} are below 0.1 and most a are between 0.2 and 1, which correspond to typical values of optical thickness and Ångström exponent for marine aerosols [*Smirnov et al.*, 1995] in open ocean. Despite the occurrence of some cases with $a > 1$ - which could correspond to BB aerosols events - no such event has been encountered using the approach described here above.

[24] Figure 5a shows the histogram of the BER_{355} (LR_{355}) retrieved during the MACAMOZ campaign for the whole troposphere. The mean BER_{355} (LR_{355}) is 0.039 sr^{-1} (26 sr) with a variability of 0.009 sr^{-1} (6 sr). The sources of uncertainties are discussed in section 4.2.

[25] The mean value of $BER_{355} = 0.039$ sr^{-1} (mean $LR_{355} =$ 26 sr) is used to assess the vertical profile of aerosol extinction coefficient in the MBL during the campaign (Figure 4, bottom left). No extinction is given below the full-overlap height (120 m, Figure 1). One can observe that the MBL aerosol layer extends up to ~0.7 km above mean sea level (amsl). This result agrees with the works of *Flamant*

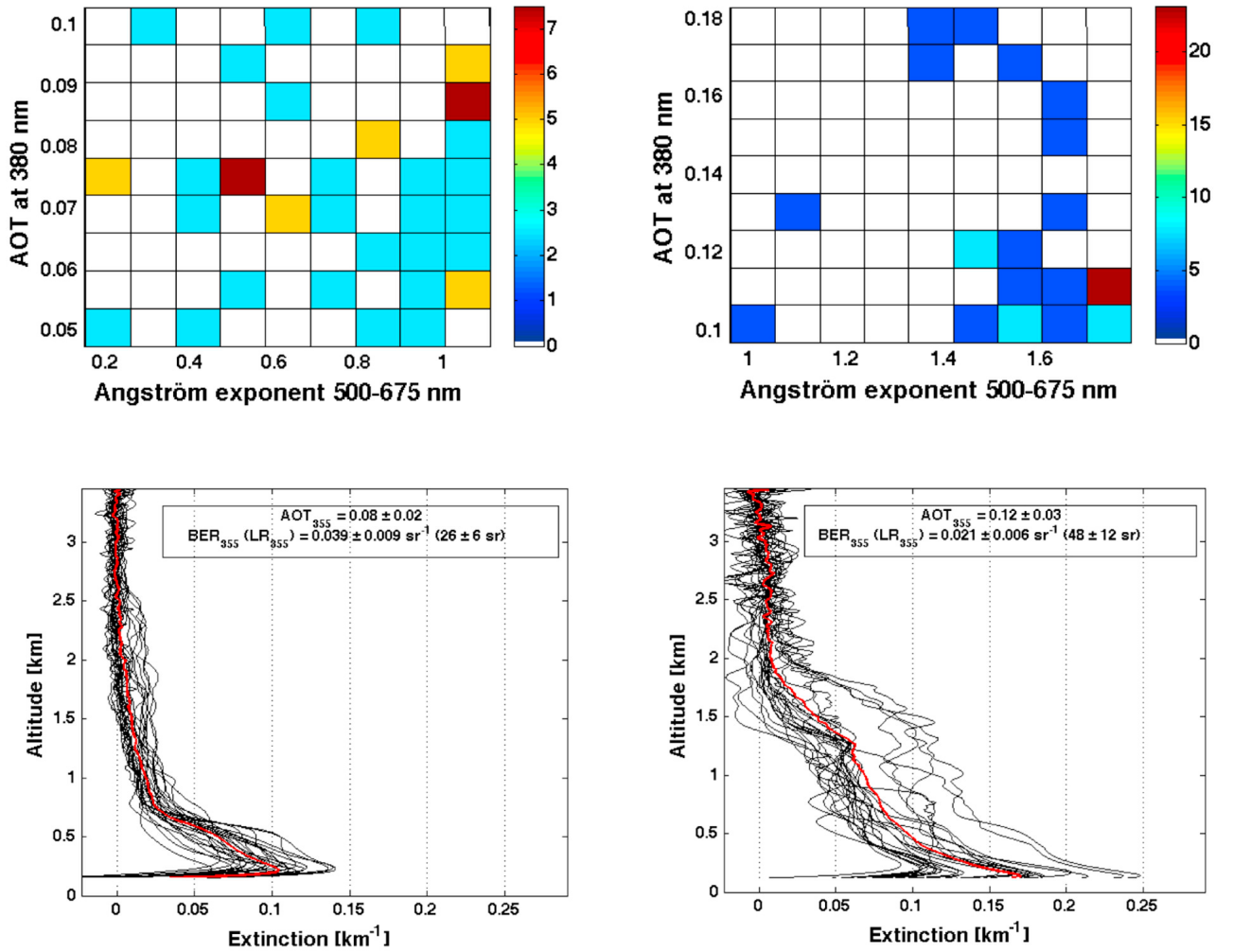

Figure 4. (left) MACAMOZ campaign; (right) KAMASUTRA campaign. (top) Cross histogram of the AOT at 380 nm and the Ångström exponent between 500 and 675 nm (relative occurrence in [%], 26 measurements for each campaign). (bottom) Aerosol extinction coefficient profiles (black) and mean aerosol extinction coefficient profile (red).

et al. [1998], *Russell et al.* [1998], and *Welton et al.* [2002] showing a MBL height in open ocean between ~0.45 and ~1 km.

3.2.2. KAMASUTRA Campaign: Optical Properties of the Biomass Burning Aerosols

[26] The KAMASUTRA campaign was characterized by almost steady cloudy conditions. However, using the same approach as described here above (Section 3.2), a BB aerosols plume event was identified during the campaign between 14th and 16th September from (31°S, 69°E) to (24°S, 59°E). We focus in this section on the data collected during the crossing of this BB plume. We use two different methods to constrain the lidar data inversion: we first use simultaneously acquired Sun photometer measurements (Section 3.2.2.1) and we then use calibration values to derive AOT at times without Sun photometer, such as nighttime (Section 3.2.2.2).

[27] We assume hereafter that the marine aerosols are mixed with the BB aerosols above, i.e., that the MBL is not isolated from the free troposphere. The validity of this hypothesis depends on the amount of turbulence at the layer interface [*Russell et al.*, 1998]. As we do not have data giving information on the (un)stability of the interface MBL-free troposphere, we chose to consider the most observed case in open ocean: the mixing between the two layers [*Russell et al.*, 1998; *Rasch et al.*, 2001; *Bates et al.*, 2002; *Welton et al.*, 2002; *Forêt et al.*, 2006]. Thus, we consider in the following a single aerosol layer containing mixed marine and BB aerosols.

3.2.2.1. Using Sun Photometer Measurements

[28] Figure 5 (top right) shows the synthesis of the Sun photometer measurements during the BB aerosols plume event using AOT_{380} and a as two independent variables. Over this period, the vessel track crossed a BB aerosol plume associated with $AOT_{380} = 0.12 \pm 0.03$ and $a = 1.52 \pm 0.21$.

[29] Figure 5b shows the histogram of the BER_{355} (LR_{355}) retrieved during the crossing of the BB aerosol plume (14–16 September) using the Sun photometer-derived AOT_{355} as a constraint for the inversion. A mean BER_{355} (LR_{355}) value of

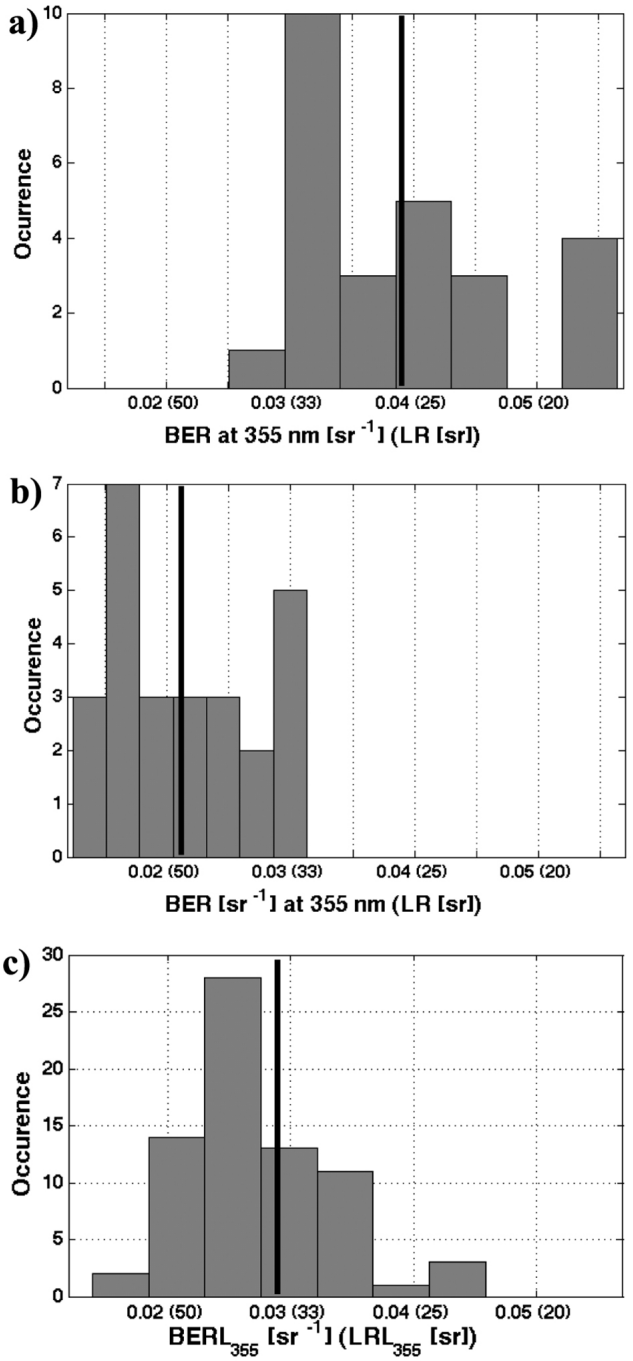

Figure 5. (a) Histogram of the BER_{355} (LR_{355}) retrieved during the MACAMOZ campaign. The mean BER_{355} (0.039 sr^{-1}) (mean LR_{355} = 26 sr) is given by the black vertical bar. (b) Histogram of the BER_{355} retrieved during the crossing of the BB aerosol plume (14–16 September – KAMASUTRA campaign). The mean BER_{355} (0.021 sr^{-1}) (mean LR_{355} = 48 sr) is given by the black vertical bar. (c) Histogram of the $BERL_{355}$ (LRL_{355}) retrieved during the crossing of the BB plume (14–16 September - KAMASUTRA campaign). The mean $BERL_{355}$ (0.029 sr^{-1}) (mean LRL_{355} = 34 sr) is given by the black vertical bar.

0.021 sr^{-1} (48 sr) with a variability of 0.006 sr^{-1} (12 sr) has been calculated for the whole troposphere. As previously, the sources of uncertainties are discussed in section 4.2. This value is significantly different from the previous BER_{355} (LR_{355}) value determined during MACAMOZ campaign for marine aerosols ($BER_{355} = 0.039 \pm 0.009$ sr^{-1} or $LR_{355} = 26 \pm 6$ sr). Comparing Figures 5a and 5b, one can see that the distributions of retrieved BER_{355} (LR_{355}) values are different, with little to no overlap between the two distributions.

[30] The mean value of BER_{355} = 0.021 sr^{-1} (LR_{355} = 41 sr) is used to assess the vertical profile of aerosol extinction coefficient during the crossing of the BB aerosol plume (14–16 September). The mean aerosol extinction coefficient profile observed during the BB aerosol event is given in Figure 5 (bottom right). No extinction is given below the full-overlap height (120 m, Figure 1). One can observe that the marine+BB aerosol (MIX aerosol) layer extends up to ~2 km amsl. This result is in accordance with the results of *Ramanathan et al.* [2001] showing that aerosol layers can extend as high as 3 km above the Indian Ocean.

3.2.2.2. Using Calibration Values to Derive AOT

[31] In this section, lidar data are inverted using the same dichotomous approach as in the previous section, except that the constraining AOT_{355} is not the Sun photometer-derived AOT acquired simultaneously with the lidar signal, but the AOT-lidar ($AOTL_{355}$) retrieved via lidar calibration (Section 3.1):

$$AOTL_{355} = \frac{1}{2}\left[\ln\frac{C_\lambda.\beta^m_{355}(z_m)}{S(z_m).(z_0 - z)^2}\right] - \tau^m_{355}(z_m) \qquad (5)$$

We still focus here on the section of the track crossing the BB aerosol plume. Figures 6a gives the histogram of the retrieved $AOTL_{355}$. A mean $AOTL_{355}$ value of 0.12 with a variability of 0.05 has been calculated. Figure 6b shows the correlation plot between $AOTL_{355}$ and AOT_{355}. The correlation coefficient equals 0.88 (26 points), which shows that the two approaches give consistent results. Moreover, whereas Figure 6b shows some discrepancies between $AOTL_{355}$ and AOT_{355} values due to uncertainties on C_λ (see Section 4.2 for discussion on uncertainties), the mean $AOTL_{355}$ value equals the mean AOT_{355} one (0.12).

[32] Derived $AOTL_{355}$ values allow us to inverse lidar data without any simultaneous Sun photometer measurements, especially lidar data acquired during nighttime. Such an extrapolation to nighttime measurements is possible because the lidar is implemented in an air-conditioned box, which avoids drifts of laser energy due to variation of temperature. We can thus reasonably suppose that the calibration constant does not change between daytime and nighttime measurements. Figure 5c shows the histogram of the $BERL_{355}$ (LRL_{355}) calculated with the $AOTL_{355}$ retrieved during the 14–16 September period. $BERL_{355}$ (LRL_{355}) values have been averaged over ten values in order to reduce the statistical error on the retrieved $BERL_{355}$ (LRL_{355}) (Section 4.2), which gives one $BERL_{355}$ (LRL_{355}) value every ~20 min. Cloudy profiles were removed from the data set. For 80% of the remaining profiles, the procedure has been convergent and a mean $BERL_{355}$ (LRL_{355}) value of 0.029 sr^{-1} (34 sr) with a variability of 0.006 sr^{-1} (7 sr) has been calculated for the whole troposphere. Such a value is within the error bar of the

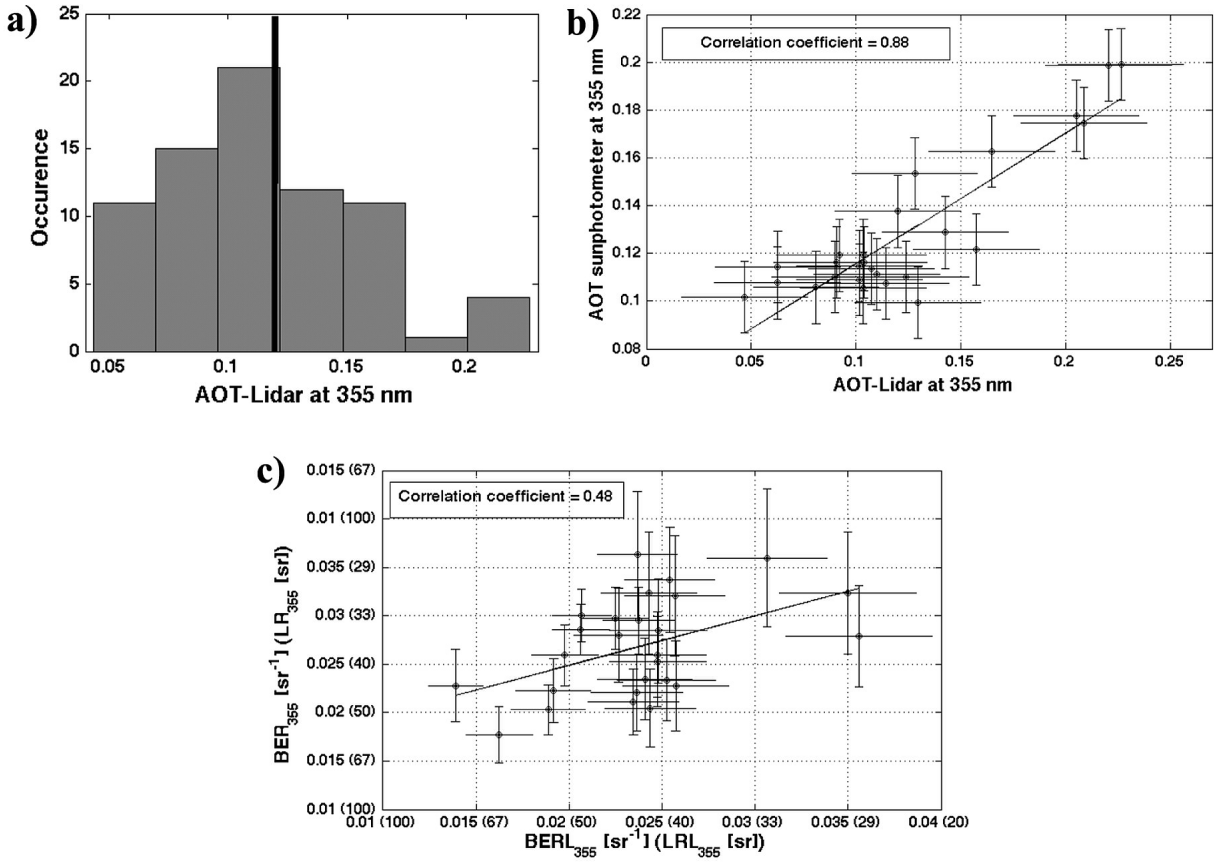

Figure 6. (a) Histogram of the $AOTL_{355}$ derived from lidar measurements and calibration. The mean $AOTL_{355}$ (0.12) is given by the black vertical bar. (b) Correlation plot between the $AOTL_{355}$ derived from lidar calibration values versus the AOT_{355} retrieved from Sun photometer measurements. The correlation coefficient equals 0.88 (26 points). (c) Correlation plot between $BERL_{355}$ (LRL_{355}) versus the BER_{355} (LR_{355}). The correlation coefficient equals 0.48 (26 points). All data were acquired during the crossing of the BB aerosol plume (14–16 September). See Section 4.2 for error bars calculation.

one deduced from the synergy between lidar and Sun photometer (see Section 4.2 for uncertainties calculation). However, the correlation coefficient between BER_{355} (LR_{355}) and $BERL_{355}$ (LRL_{355}) is 0.48 (26 points, Figure 6c), which is lower than the one between $AOTL_{355}$ and AOT_{355} (0.88). This can be explained by the high sensitivity of the BER retrieval technique to the value of the AOT used to constrain the inversion (see Section 4.2). Investigating the distribution of the retrieved $BERL_{355}$ (LRL_{355}) (Figure 5c), one can notice some cases with $BERL_{355} > 0.030$ ($LRL_{355} < 33$), which implies that the crossed plume is not uniformly loaded in aerosols. These high (low) values of $BERL_{355}$ (LRL_{355}) may also result from underestimated $AOTL_{355}$ (Figure 6b).

[33] Figure 7a shows the evolution with time of AOT_{355} and $AOTL_{355}$ during the crossing of the BB plume (values of error bars are explained in Section 4.2). One can see that AOT_{355} and $AOTL_{355}$ values are within each other's error bars. $AOTL_{355}$ values stay between 0.05 and 0.13 on the 14/09, increase to 0.2 on the 15/09 and stay around 0.15 on the 16/09. Figure 7b shows the evolution with time of the retrieved BER_{355} (LR_{355}) and $BERL_{355}$ (LRL_{355}) during the crossing of the BB plume (see Section 4.2 for the error bars calculation). One can see that BER_{355} (LR_{355}) and $BERL_{355}$ (LRL_{355}) values are within each other's error bars. $BERL_{355}$ (LRL_{355}) evolves mostly between ~0.025 and ~0.045 sr^{-1} (~22–40 sr) on the 14/09, decreases (increases) to ~0.02 sr^{-1} (~50 sr) on the 15/09, and finally stays between ~0.02 and ~0.03 sr^{-1} (~33–50 sr) on the 16/09. It seems therefore that the part of the plume crossed on the 15/09 is the one containing the more BB aerosols (highest $AOTL_{355}$ and lowest $BERL_{355}$). One can also note that $BERL_{355}$ (LRL_{355}) decreases (increases) while $AOTL_{355}$ increases: the correlation coefficient between $BERL_{355}$ and $AOTL_{355}$ is −0.60 (72 points, Figure 7c). This suggests that the increase of the optical thickness is mainly due to the increase of the BB aerosol concentration.

[34] Three extinction profiles (one per day) have been selected and are shown in Figure 8 (no extinction is given below the full-overlap height of 120 m as shown in Figure 1). We chose extinction profiles coinciding with Sun photometer measurements to compare the results obtained from the two retrieval methods (Sun photometer measurements versus calibration values). The related time, $AOTL_{355}$, AOT_{355}, $BERL_{355}$ and BER_{355} are shown for each profile. One can first

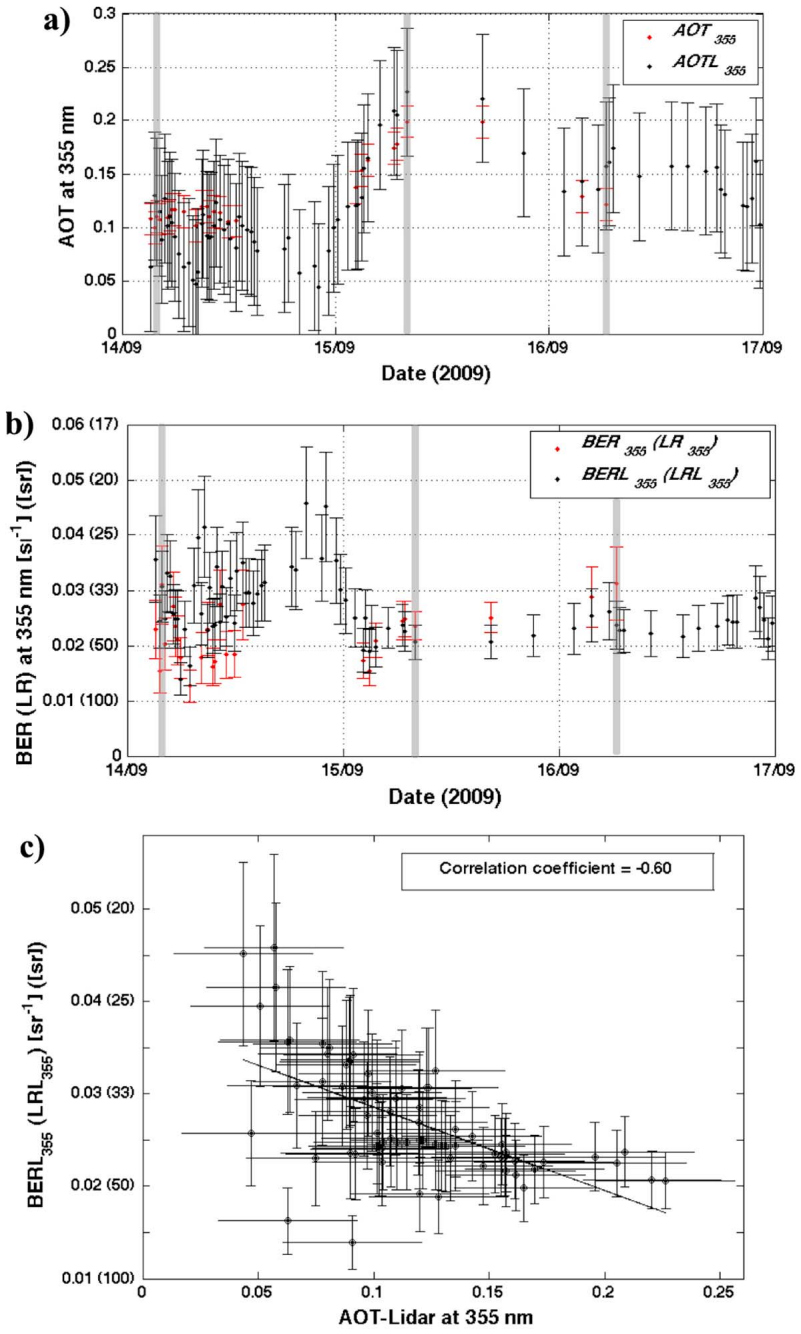

Figure 7. (a) Temporal evolution of the retrieved AOT_{355} and $AOTL_{355}$ during the crossing of the BB plume. The error bars are also given. (b) Temporal evolution of the retrieved BER_{355} and $BERL_{355}$ during the crossing of the BB plume. The gray bars stand for the extinction profiles shown in Figure 8. (c) Correlation plot between the $BERL_{355}$ (LRL_{355}) versus the $AOTL_{355}$. The correlation coefficient equals −0.60 (72 points). See Section 4.2 for error bars calculation.

notice that the shapes of the extinction profiles retrieved using the calibration values to derive the $AOTL_{355}$ are in quite good accordance with the shape of the extinction profiles retrieved using Sun photometer measurements (AOT_{355}). However, the selected profiles show a slightly higher extinction when retrieved via $AOTL_{355}$. This can be explained by the fact that the related $AOTL_{355}$ are slightly higher than the related AOT_{355} for the selected cases.

[35] The height of the aerosol layer is ~1.8 km on the 14/09 profile (Figure 8a), ~3 km on the 15/09 profile (Figure 8b) and ~2.5 km on the 16/09 profile (Figure 8c). This result is also in accordance with the results of *Ramanathan et al.* [2001] showing that aerosol layers can extend as high as 3 km above the Indian Ocean. The 15/09 profile (Figure 8b) shows an enhanced aerosol layer between ~0.7 and ~1.4 km amsl, which could be related to the highest $AOTL_{355}$ and

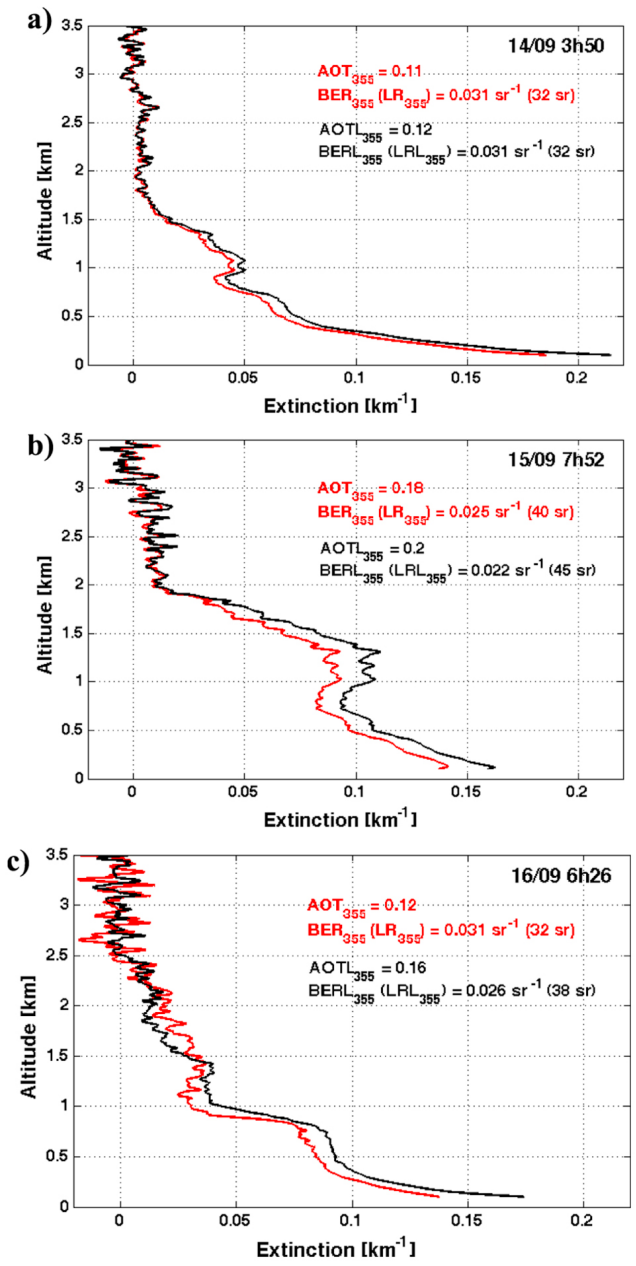

Figure 8. Aerosol extinction coefficient profiles retrieved from lidar and Sun photometer measurements (red) and aerosol extinction coefficient profiles retrieved from lidar measurements using calibration values to derive $AOTL_{355}$ (black) on (a) 14/09 3h50, (b) 15/09 7h52, and (c) 16/09 6h26. Times are Universal Time (UT).

lowest (highest) $BERL_{355}$ (LRL_{355}) observed on the 15/09 (Figure 7). This layer is therefore likely to contain mostly BB aerosols.

4. Discussion

4.1. Origin of the Aerosol Loaded Air Masses: Comparison With the GIRAFE Model

[36] The mean tropospheric lifetime of BB aerosols is usually estimated being in the 4 to 7 days range [*Andreae*, 1995; *Rasch et al.*, 2000; *Edwards et al.*, 2006]. In order to take into account long-range transports of aerosol plumes, seven days forward GIRAFE simulations were performed for each day from 7 to 15 September in order to compare GIRAFE results and lidar-Sun photometer observations for the 14–16 September period and to identify the origin of the air masses. Particles were emitted up to 2000 m agl (Section 2.2) for each fire pixel detected by MODIS (Section 2.1.4 and 2.2). Geographical and height (agl) distributions of the particles remaining in the troposphere between the 14 and 16 September have been averaged in a 1° × 1° gridded map on this three day period (Figure 9). Note that the geographical distribution of the particles (number of particles in a 1° × ° square) is given in a log scale. The extreme ship positions during the investigated period ([31°S, 68°E] and [24°S, 59°E]) are highlighted by the black crosses. Five main BB plumes can be identified in Figure 9: one plume exiting off southeast South America, crossing the South Atlantic ocean and joining the second plume exiting off South-Southeast Africa and Madagascar toward Australia, a third one exiting off Indonesia-Malaysia toward the southwestern Indian Ocean, a fourth exiting off northwest Australia and joining the Indo-Malaysian plume, and a fifth one exiting off northwest southern Africa toward South America. This simulated BB plume distribution is in accordance with previous studies on Southern Hemisphere pollution transportation patterns such as those by *Annegarn et al.* [2002] and *Edwards et al.* [2006]. Moreover, the long-range transport pathway at high tropospheric altitude from Southeast Asia and Indonesia-Malaysia toward the southwestern Indian Ocean is clearly visible in Figure 9b, showing a transportation altitude of ~13 km [*Duflot et al.*, 2010].

[37] One can see that the ship is on the edge of the BB plume during this period and almost at the junction between the BB plumes coming from South America, Southern Africa and Southeast Asia. This confirms the BB origin of the encountered aerosol plume and can explain the relatively low AOT_{355} measured during the crossing of the plume (~0.1–0.2). To assess the relative contribution of each of the BB emission areas (South America, Southern Africa and Asia-Oceania) to the detected BB aerosol plume, we performed the same set of simulations separately for each of these three areas and counted the number of particles forming the detected plume. The resulting relative contributions are: 50% from South America, 44% from Southern Africa and 6% from Asia-Oceania. This agrees with the work of *Duflot et al.* [2010] showing that the area contributing the most to the pollutant concentration in the Réunion Island area (21°S, 55°E), which is ~600 km to the location of the detected BB plume, is South America in September. However, the relative contributions by area calculated in our present work should be considered carefully for the following reasons: 1) the same number of particles was emitted from each fire, independently from the type of biomass burnt; 2) emitted particles were uniformly distributed in altitude and emitted at the same injection height (2 km agl), independently from the location of the fire; 3) the processes affecting aerosols during their transportation were not taken into account, such as chemical reactions, growth and resulting deposition. These two last limitations of the model should also be taken into account in the exploitation of the simulated vertical distribution of the aerosols. One can see in Figure 9b that the simulated mean

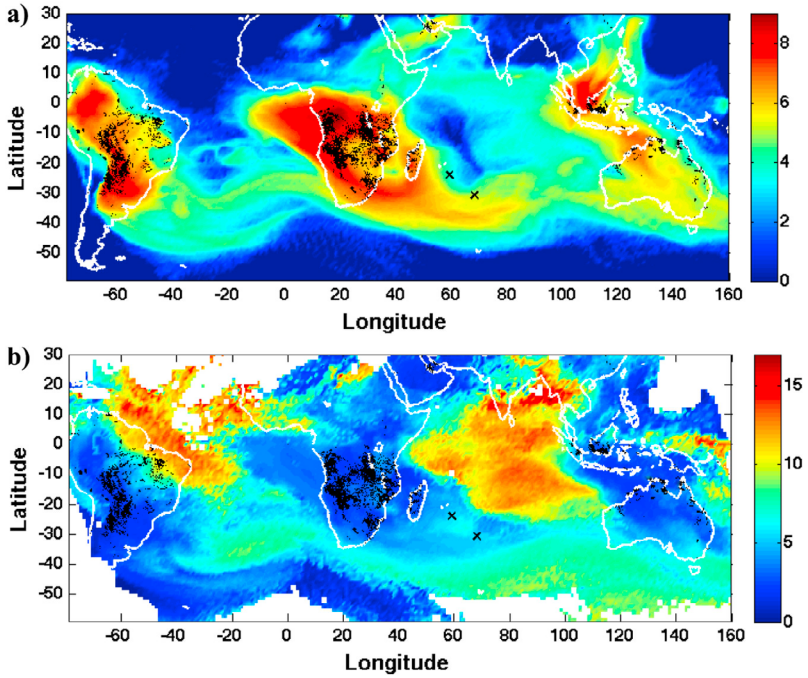

Figure 9. 1° × 1° averaged particles (a) geographical [arbitrary unit] and (b) height [km] distributions for particles remaining in the atmosphere between 14 and 16 September, 2009 for 7 days GIRAFE simulations from 7 to 15 September, 2009. Black dots are fires detected by MODIS and black crosses are extreme ship positions on 14 and 16 September, 2009 ([31°S, 69°E] and [24°S, 59°E]).

particles height between the two extreme ship positions is around 6 km amsl, which is not in accordance with the aerosol layer height observed from lidar measurements (up to ~2.7 km, Figures 4 and 8). It seems therefore that the GIRAFE model is a powerful tool to simulate the horizontal distribution of BB aerosols, but is not suitable to simulate their height distribution. A new version of GIRAFE (v4) using the FLEXPART 8.2 model should be released soon. More detailed settling parameterization for aerosols is implemented in the FLEXPART 8.2 model, which should improve the ability of GIRAFE to simulate BB aerosols height distribution.

4.2. Uncertainties on the Retrieved BER Values

[38] A direct-inverse model has been developed in order to assess uncertainties on the retrieval of marine and biomass burning aerosol optical properties.

[39] In case of marine aerosol (Section 3.2.1) a Gaussian aerosol layer has been simulated between 0 and 0.7 km amsl with an AOT_{355} of 0.08 and a BER_{355} of 0.039 sr^{-1} corresponding to the mean values observed during MACAMOZ campaign. Four sources of uncertainties have been identified: i) the uncertainty on the a priori knowledge of the vertical profile of the molecular backscatter signal, ii) the uncertainty on the lidar signal in the altitude range used for the normalization, iii) the statistical fluctuations in the lidar signal associated with random detection processes and iv) the uncertainty on AOT used to constraint lidar inversion (0.015, Section 2.1.2). The uncertainty on the a priori knowledge of the molecular contribution has been assessed to be lower than 2% [*Chazette et al.*, 2010] using a comparison between several vertical sounding (i.e., radiosounding). The uncertainty on the lidar signal in the altitude range used for the normalization has been assessed to be lower than 6% [*Royer et al.*, 2011]. The statistical fluctuation in the lidar signal is here neglectable as Signal-to-Noise ratio of range-corrected signal is ~100 at the reference. The uncertainty due to AOT value has been assessed using a Monte Carlo approach as in *Chazette et al.* [2001] with 1000 realizations assuming a normal probability density function with a standard deviation of 0.015 around different values of AOT_{355}. Figure 10a shows the relative uncertainty on the retrieved BER for marine aerosols as a function of the AOT_{355}. The standard deviation of 0.015 on AOT_{355} has been found to be the major source of uncertainty (between 87 and 97% of total uncertainty). The different sources of uncertainty have been supposed to be independent which lead to an overall uncertainty corresponding to 18 to 36% (~ 0.007 to 0.014 sr^{-1}) of error on BER_{355} values for marine aerosols for a mean AOT_{355} of 0.12 and 0.04 respectively. The mean uncertainty on BER_{355} for marine aerosols equals 0.009 sr^{-1} (6 sr).

[40] In case of the mixing between BB and marine (MIX) aerosols (Section 3.2.2) a Gaussian aerosol layer has been simulated between 0 and 2 km amsl with an AOT_{355} of 0.12 and a BER_{355} of 0.021 sr^{-1} corresponding to the mean values observed during the crossing of the BB plume during the KAMASUTRA campaign. The same four sources of uncertainties as in the case of marine aerosols have been identified. Figure 10b shows the relative uncertainty on the retrieved BER for MIX aerosols as a function of the AOT_{355}. The standard deviation of 0.015 around the values of

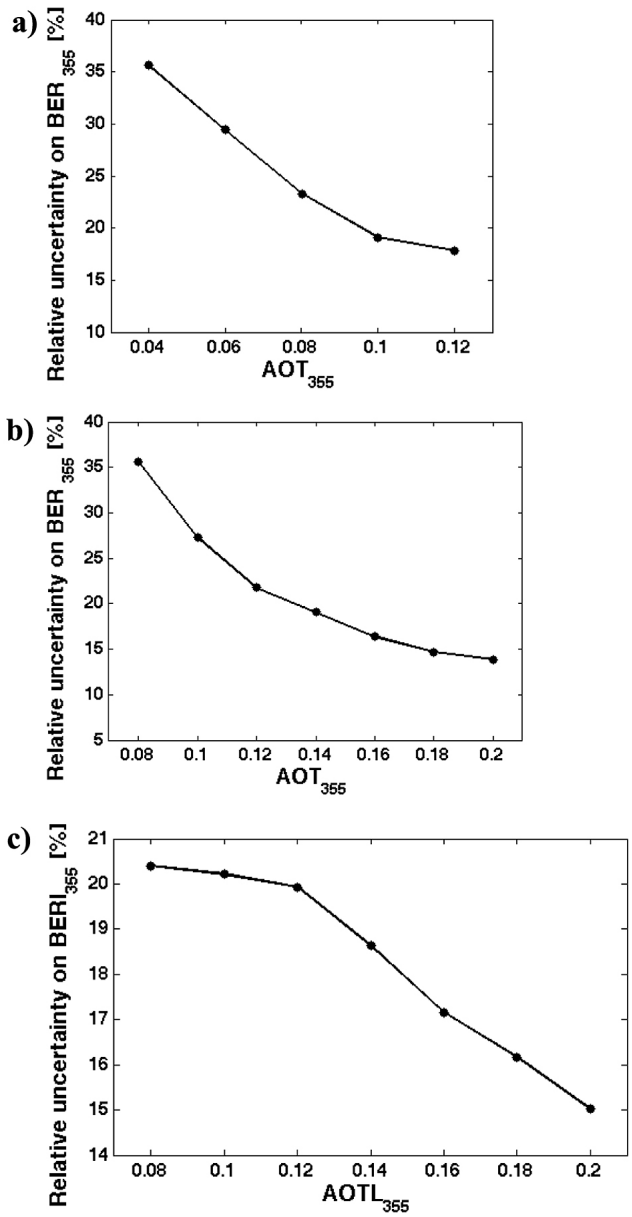

Figure 10. (a) Relative uncertainty on the retrieved BER_{355} as a function of the AOT_{355} for the marine aerosols. (b) Relative uncertainty on the retrieved BER_{355} as a function of the AOT_{355} for the MIX aerosols. (c) Relative uncertainty after temporal averaging on the retrieved $BERL_{355}$ as a function of the $AOTL_{355}$ for the MIX aerosols.

AOT_{355} has been found to be the major source of uncertainty (between 80 and 97% of total uncertainty). The different sources of uncertainty have been supposed to be independent which lead to an overall uncertainty corresponding to 14 to 36% (~ 0.003 to 0.008 sr^{-1}) of error on BER values for MIX aerosols. The mean uncertainty on BER_{355} (LR_{355}) for the mixed marine and BB aerosols equals 0.004 sr^{-1} (9 sr).

[41] In case of $BERL_{355}$ retrieved thanks to the instrumental constant C_λ through $AOTL_{355}$ for MIX aerosols (Section 3.3), a Gaussian aerosol layer has been simulated between 0 and 2 km amsl with an $AOTL_{355}$ of 0.12 and a $BERL_{355}$ of 0.029 sr^{-1} corresponding to the mean values retrieved during the crossing of the BB plume. One additional source of uncertainty has to be considered in this case: relative uncertainty on C_λ (12%) which leads to an uncertainty on $AOTL_{355}$ of 0.06. In order to reduce the induced uncertainty on the retrieved $BERL_{355}$, lidar profiles have been averaged over ten profiles. Uncertainty on $AOTL_{355}$ has been found to be the major source of uncertainty (>98% of total uncertainty on $BERL_{355}$). $BERL_{355}$ have been averaged over 10 profiles in order to reduce the uncertainty of the retrieval. Figure 10c shows the final relative uncertainty after temporal averaging on the retrieved $BERL_{355}$ for MIX aerosols as a function of the $AOTL_{355}$. The different sources of uncertainty have been supposed to be independent which lead to an overall uncertainty corresponding to 15 to 20% (~ 0.004 to 0.006 sr^{-1}) of error on BER values for MIX aerosols. The mean uncertainty on $BERL_{355}$ (LRL_{355}) for the mixed marine and BB aerosols equals 0.005 sr^{-1} (6 sr).

4.3. Comparison With Other Studies

[42] Table 1 shows retrieved BER_λ (LR_λ) values from previous studies for BB and marine aerosols, as well as the used lidar wavelengths and the measurement (for marine aerosols) and source (for marine+BB aerosols) areas. Table 1 is not exhaustive, but rather a summary of what can be found in the literature about BER_λ (LR_λ) for marine aerosols and for BB aerosols coming from Southern Africa and South America. The values presented in Table 1 are from direct ground based lidar measurements that do not rely on assumptions of particle composition, shape, or size (except for data from *Cattrall et al.* [2005]). Note that no values of BER_{355} for marine aerosols or for BB aerosols coming from Southern Africa have been found in the literature. Considering the weak spectral dependence (low a) of marine aerosols in the UV and visible spectral domains, the values retrieved in the frame of this study are in agreement with the results of previous works. The mean BER_{355} (LR_{355}) of 0.039 ± 0.009 sr^{-1} (26 ± 6 sr) we derived for marine aerosols is nearly identical to the mean of those previously retrieved, which go from BER_{523} = 0.030 ± 0.005 sr^{-1} (LR_{523} = 33 ± 6 sr) [*Welton et al.*, 2002] to BER_{532} = 0.043 ± 0.009 sr^{-1} (LR_{532} = 23 ± 5 sr) [*Müller et al.*, 2007], both in the tropical northern Indian Ocean.

[43] Previous retrieved BER_{355} (LR_{355}) values for Eastern European BB aerosols range from 0.015 ± 0.006 sr^{-1} (70 ± 30 sr) [*Amiridis et al.*, 2009] to 0.017 sr^{-1} (59 sr) [*Balis et al.*, 2003]. *Chazette et al.* [2007] give BER_{355} (LR_{355}) of 0.008 ± 0.003 sr^{-1} (125 ± 35 sr) over southern Niger. For Southern African BB aerosols, previously retrieved BER_λ (LR_λ) values range from 0.016 ± 0.003 sr^{-1} (63 ± 10 sr) [*Campbell et al.*, 2003] to 0.017 ± 0.002 sr^{-1} (60 ± 8 sr) [*Cattrall et al.*, 2005] at λ = 523 and 550 nm, respectively.

[44] One can see that our retrieved BER_{355} (LR_{355}) for BB aerosols mainly coming from Southern Africa and South America and mixed with marine aerosols is within the range of the BER (LR) retrieved at 355 nm for BB aerosols coming from Eastern Europe, but slightly above (below) the range of the previously retrieved BER_λ (LR_λ) at higher λ (523 and 550 nm) for Southern African BB aerosols. This can be explained by the fact that, oppositely to these previous studies, the detected BB aerosol plume is encountered more

Table 1. Retrieved BER_λ (and LR_λ) From Previous Ground Based Studies for BB and Marine Aerosols

Reference	Wavelength [nm][a]	Marine Aerosols		BB Aerosols	
		BER [sr^{-1}] (LR [sr])[b]	Measurement Area[c]	BER [sr^{-1}] (LR [sr])[d]	Source Area[e]
Flamant et al. [1998]	532	0.041 ± 0.008 (24 ± 5)	North Atlantic		
Franke et al. [2001]	532	>0.033 (<30)	Northern Indian Ocean		
Müller et al. [2001]	532	0.040 (25)	Northern Indian Ocean		
Welton et al. [2002]	523	0.030 ± 0.005 (33 ± 6)	Tropical Indian Ocean		
Cattrall et al. [2005]	550	0.036 ± 0.006 (28 ± 5)	Global	0.017 ± 0.002 (60 ± 8)	South America and Southern Africa
Müller et al. [2007]	532	0.043 ± 0.009 (23 ± 5)	Northern Indian Ocean	0.019 ± 0.004 (53 ± 11)	Siberia/Canada
Müller et al. [2007]	**355**[f]			0.022 ± 0.006 (46 ± 13)	Siberia/Canada
Balis et al. [2003]	**355**			0.017 (59)	Eastern Europe
Campbell et al. [2003]	523			0.013 ± 0.003 (63 ± 10)	Southern Africa
Chazette et al. [2007]	**355**			0.008 ± 0.003 (125 ± 35)	Niger
Amiridis et al. [2009]	**355**			0.015 ± 0.006 (70 ± 30)	Eastern Europe
This study	**355**	0.039 ± 0.009 (26 ± 6)	Southwestern Indian Ocean	0.021 ± 0.006 (48 ± 12)	South America and Southern Africa

[a]The wavelength λ at which the BER_λ (and LR_λ) were retrieved.
[b]The mean BER_λ (and LR_λ) for marine aerosols with the associated standard deviation.
[c]The marine aerosols measurement area.
[d]The mean BER_λ (and LR_λ) for BB aerosols with the associated standard deviation.
[e]The identified BB aerosols source area.
[f]Boldfacing indicates studies that used the same lidar wavelength as this study.

than 2500 km from its emission area, and thus can be affected by changing of the particles optical properties during the transportation. *Müller et al.* [2007] retrieved a BER_{355} (LR_{355}) value of 0.022 ± 0.006 sr^{-1} (46 ± 13 sr) – which is very close to our value - over Europe for BB aerosol plume coming from Siberia/Canada. They state that long-range transport of aerosols seems to increase (decrease) the BER (LR). This may be due, in our case, to mixing with marine particles over the South Atlantic and Southern Indian Ocean, particle growth due to uptake of water or precursor gases, photochemical reactions, and particle growth because of coagulation. This can explain the difference with the BER_{355} (LR_{355}) retrieved over Southern Niger by *Chazette et al.* [2007]. We must also consider that the present study is actually the first report (to our knowledge) on the characterization of the aerosols optical properties over the southern Indian Ocean from ground-based mobile lidar measurements, thus reference data are missing.

[45] Figure 11 displays a summary of the Ångström coefficient between 500 and 870 nm (a) versus the BER_{355} (LR_{355}) retrieved from the synergy between the lidar and the Sun photometer (Section 3.2.1 and 3.2.2.1). The BER_{355} (LR_{355}) boundary between the "marine" and "MIX" (BB+marine) types is the minimum (maximum) BER (LR) value found in the literature for marine aerosols (BER = 0.030 sr^{-1} and LR = 33 sr found by *Welton et al.* [2002] at 523 nm). The signatures of marine and MIX aerosols are well identified because little to no overlap is observed. Marine aerosols BER_{355} (LR_{355}) and a range from 0.030 to 0.057 sr^{-1} (18–33 sr) and from 0.10 to 0.95, respectively, while MIX aerosols BER_{355} (LR_{355}) and a range from 0.012 to 0.030 sr^{-1} (33–83 sr) and from 0.86 to 1.51, respectively. This is in accordance with the work of

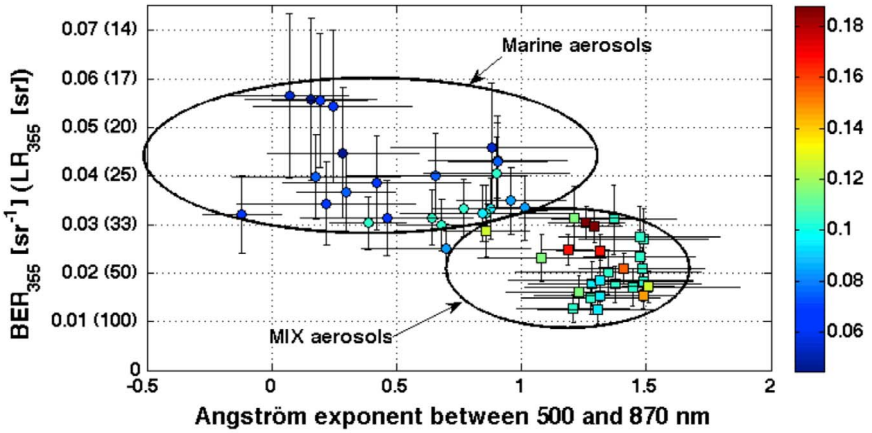

Figure 11. Ångström exponent between 500 and 870 nm versus retrieved BER at 355 nm for marine aerosols (MACAMOZ campaign, circles) and MIX aerosols (KAMASUTRA campaign, squares). Error bars on BER_{355} are from uncertainty described in Section 4.2. Error bars on Ångström exponent are from uncertainty on AOT and have been computed following a similar approach showed by *Hamonou et al.* [1999]. The gray scale gives related AOT at 380 nm.

Cattrall et al. [2005] showing a clear separation between the BER related to BB and marine aerosols. One can verify also in Figure 11 that the AOT related to BER of MIX aerosols are higher than the AOT related to BER of only marine aerosols.

5. Conclusion

[46] Lidar observations were performed on the research vessel Marion Dufresne during two ship-based opportunity experiments: one around Madagascar in late austral summer 2009 and one between La Réunion (21°S, 55°E) and the Kerguelen Islands (50°S, 70°E) in austral winter (Southern Hemisphere BB season) 2009. A BB aerosol layer has been encountered between (31°S, 69°E) and (24°S, 59°E) in mid September 2009. The Sun photometer-derived AOT_{355} has been used as a constraint to determine the mean BER_{355} (LR_{355}) in the marine aerosol layer as well as in the mixed BB+marine aerosol layer, and leads to mean value of 0.039 ± 0.009 sr^{-1} (26 ± 6 sr) and 0.021 ± 0.006 sr^{-1} (48 ± 12 sr), respectively. The mean aerosol extinction profile has been calculated which reveals an aerosol layer extending up to ~3 km amsl. Lidar calibration is used to inverse data without any simultaneous Sun photometer measurements (as nighttime data) and the time evolution of the aerosol extinction properties and vertical extension are documented. We used the GIRAFE/FLEXPART model to confirm the BB origin of the detected aerosol layer: the encountered aerosol plume comes mainly from BB occurring in South America and Southern Africa. However, the mean height of the encountered plume as simulated by GIRAFE is not in agreement with the altitude of the detected aerosol layer. Further studies should be performed with the next version of GIRAFE-FLEXPART (v4), which includes additional aerosols parameterization. This first (to our knowledge) direct ground-based mobile measurement of the aerosols characteristics and spatial distribution in the southern Indian Ocean can be useful for reducing uncertainties in the global climate models for the southern hemisphere.

[47] **Acknowledgments.** The MACAMOZ and KAMASUTRA campaigns were supported by the French Polar Institute (IPEV) and the Marion Dufresne is property of the Terres Australes et Antarctiques Françaises (TAAF). The Centre National de Recherche Scientifique (CNRS) and the Agence de l'Environnement et de la Maîtrise de l'Energie (ADEME) provide funding to V. Duflot for his Ph.D. This study has been supported by the program Les Enveloppes Fluides et l'Environnement-Chimie Atmosphérique (LEFE-CHAT) of the Institut National des Sciences de l'Univers (INSU-CNRS). We thank the ECMWF center for supplying global model data. We acknowledge the MODIS mission scientists and associated NASA personnel, as well as the Giovanni online data system, developed and maintained by the NASA GES DISC, for providing MODIS AOT data. We also thank the University of Maryland for providing fires detection data. GIRAFE is supported by ETHER (CNES and INSU-CNRS). Franck Gabarrot, Martial Barblu and Patrick Hernandez also receive our gratitude for supporting the LIDAR and Sun photometer operation during the MACAMOZ campaign. We also wish to thank Franck Gabarrot for his participation in the GIRAFE model testing and set up.

References

Amiridis, V., D. S. Balis, E. Giannakaki, A. Stohl, S. Kazadzis, M. E. Koukouli, and P. Zanis (2009), Optical characteristics of biomass burning aerosols over southeastern Europe determined from UV-Raman lidar measurements, *Atmos. Chem. Phys.*, *9*, 2431–2440, doi:10.5194/acp-9-2431-2009.

Andreae, M. O. (1995), Climatic effects of changing atmospheric aerosol levels, in *World Survey of Climatology*, vol. 16, *Future Climates of the World*, edited by A. Henderson-Sellers, pp. 341–392, Elsevier Sci., New York.

Andreae, M. O. (1996), Raising dust in the greenhouse, *Nature*, *380*, 389–390, doi:10.1038/380389a0.

Ångström, A. (1964), The parameters of atmospheric turbidity, *Tellus*, *16*, 64–75, doi:10.1111/j.2153-3490.1964.tb00144.x.

Annegarn, H. J., et al. (2002), Southern Africa's ecosystem in a test-tube-A perspective on the Southern African Regional Science Initiative (SAFARI 2000), *S. Afr. J. Sci.*, *98*, 111–113.

Balis, D. S., V. Amiridis, C. Zerefos, E. Gerasopoulos, M. Andreae, P. Zanis, A. Kazantzidis, S. Kazadzis, and A. Papayannis (2003), Raman lidar and sunphotometric measurements of aerosol optical properties over Thessaloniki, Greece during a biomass burning episode, *Atmos. Environ.*, *37*, 4529–4538, doi:10.1016/S1352-2310(03)00581-8.

Bates, T. S., D. J. Coffman, D. S. Covert, and P. K. Quinn (2002), Regional marine boundary layer aerosol size distributions in the Indian, Atlantic, and Pacific Oceans: A comparison of INDOEX measurements with ACE-1, ACE-2, and Aerosols99, *J. Geophys. Res.*, *107*(D19), 8026, doi:10.1029/2001JD001174.

Campbell, J. R., E. J. Welton, J. D. Spinhirne, Q. Ji, S.-C. Tsay, S. J. Piketh, M. Barenbrug, and B. N. Holben (2003), Micropulse lidar observations of tropospheric aerosols over northeastern South Africa during the ARREX and SAFARI 2000 dry season experiments, *J. Geophys. Res.*, *108*(D13), 8497, doi:10.1029/2002JD002563.

Cattrall, C., J. Reagan, K. Thome, and O. Dubovik (2005), Variability of aerosol and spectral lidar and backscatter and extinction ratios of key aerosol types derived from selected Aerosol Robotic Network locations, *J. Geophys. Res.*, *110*, D10S11, doi:10.1029/2004JD005124.

Chazette, P. (2003), The monsoon aerosol extinction properties at Goa during INDOEX as measured with lidar, *J. Geophys. Res.*, *108*(D6), 4187, doi:10.1029/2002JD002074.

Chazette, P., J. Pelon, and G. Mégie (2001), Determination of structural parameters of atmospheric scattering layer using spaceborne backscatter lidar, *Appl. Opt.*, *40*, 3428–3440, doi:10.1364/AO.40.003428.

Chazette, P., J. Sanak, and F. Dulac (2007), New approach for aerosol profiling with a lidar onboard an ultralight aircraft: Application to the African Monsoon Multidisciplinary Analysis, *Environ. Sci. Technol.*, *41*, 8335–8341, doi:10.1021/es070343y.

Chazette, P., J.-C. Raut, F. Dulac, S. Berthier, S.-W. Kim, P. Royer, J. Sanak, S. Loaëc, and H. Grigaut-Desbrosses (2010), Simultaneous observations of lower tropospheric continental aerosols with a ground-based, an airborne, and the spaceborne CALIOP lidar systems, *J. Geophys. Res.*, *115*, D00H31, doi:10.1029/2009JD012341.

Crutzen, P. J., and M. O. Andreae (1990), Biomass burning in the tropics: Impact on atmospheric chemistry and biogeochemical cycles, *Science*, *250*, 1669–1678, doi:10.1126/science.250.4988.1669.

Dentener, F>, et al. (2006), Emissions of primary aerosol and precursor gases in the years 2000 and 1750 prescribed data-sets for AeroCom, *Atmos. Chem. Phys.*, *6*, 4321–4344, doi:10.5194/acp-6-4321-2006.

Duflot, V., B. Dils, J. L. Baray, M. De Mazière, J. L. Attié, G. Vanhaelewyn, C. Senten, C. Vigouroux, G. Clain, and R. Delmas (2010), Analysis of the origin of the distribution of CO in the subtropical southern Indian Ocean in 2007, *J. Geophys. Res.*, *115*, D22106, doi:10.1029/2010JD013994.

Edwards, D. P., et al. (2006), Satellite-observed pollution from Southern Hemisphere biomass burning, *J. Geophys. Res.*, *111*, D14312, doi:10.1029/2005JD006655.

Flamant, C., V. Trouillet, P. Chazette, and J. Pelon (1998), Wind speed dependence of the atmospheric boundary layer optical properties and ocean surface reflectance as observed by airborne backscatter lidar, *J. Geophys. Res.*, *103*, 25,137–25,158, doi:10.1029/98JC02284.

Forêt, G., C. Flamant, S. Cautenet, J. Pelon, F. Minvielle, M. Taghavi, and P. Chazette (2006), The structure of the haze plume over the Indian Ocean during INDOEX: Tracer simulations and lidar observations, *Atmos. Chem. Phys.*, *6*, 907–923, doi:10.5194/acp-6-907-2006.

Franke, K., A. Ansmann, D. Müller, D. Althausen, F. Wagner, and R. Scheele (2001), One-year observations of particle lidar ratio over the tropical Indian Ocean with Raman lidar, *Geophys. Res. Lett.*, *28*, 4559–4562, doi:10.1029/2001GL013671.

Giglio, L., et al. (2003), An enhanced contextual fire detection algorithm for MODIS, *Remote Sens. Environ.*, *87*, 273–282, doi:10.1016/S0034-4257(03)00184-6.

Hamonou, E., P. Chazette, D. Balis, F. Dulac, X. Schneider, E. Galani, G. Ancellet, and A. Papayannis (1999), Characterization of the vertical structure of Saharan dust export to the Mediterranean basin, *J. Geophys. Res.*, *104*, 22,257–22,270.

Intergovernmental Panel on Climatic Change (2007), *Climate Change 2007: Radiative Forcing of Climate*, Cambridge Univ. Press, New York.

Kaufman, Y. J., D. Tanré, L. A. Remer, E. F. Vermote, A. Chu, and B. N. Holben (1997), Operational remote sensing of tropospheric aerosol over

land from EOS moderate resolution imaging spectroradiometer, *J. Geophys. Res.*, *102*, 17,051–17,067, doi:10.1029/96JD03988.

Klett, J. D. (1985), Lidar inversion with variable backscatter/extinction ratios, *Appl. Opt.*, *24*, 1638–1643, doi:10.1364/AO.24.001638.

Lelieveld, J., et al. (2001), The Indian Ocean Experiment: Widespread air pollution from South and Southeast Asia, *Science*, *291*, 1031–1036, doi:10.1126/science.1057103.

Léon, J.-F., et al. (2001), Large-scale advection of continental aerosols during INDOEX, *J. Geophys. Res.*, *106*, 28,427–28,439, doi:10.1029/2001JD900023.

Measures, R. M. (1984), *Laser Remote Sensing: Fundamentals and Applications*, Wiley-Interscience, New York.

Müller, D., K. Franke, F. Wagner, D. Althausen, A. Ansmann, and J. Heintzenberg (2001), Vertical profiling of optical and physical particle properties over the tropical Indian Ocean with six-wavelength lidar: 2. Case studies, *J. Geophys. Res.*, *106*, 28,577–28,595, doi:10.1029/2000JD900785.

Müller, D., A. Ansmann, I. Mattis, M. Tesche, U. Wandinger, D. Althausen, and G. Pisani (2007), Aerosol-type-dependent lidar ratios observed with Raman lidar, *J. Geophys. Res.*, *112*, D16202, doi:10.1029/2006JD008292.

Nicolet, M. (1984), On the molecular scattering in the terrestrial atmosphere, *Planet. Space Sci.*, *32*, 1467–1468, doi:10.1016/0032-0633(84)90089-8.

Pelon, J., C. Flamant, P. Chazette, J.-F. Leon, D. Tanre, M. Sicard, and S. K. Satheesh (2002), Characterization of aerosol spatial distribution and optical properties over the Indian Ocean from airborne lidar and radiometry during INDOEX'99, *J. Geophys. Res.*, *107*(D19), 8029, doi:10.1029/2001JD000402.

Pietras, C., K. D. Knobelspiesse, R. Frouin, B. Holben, and K. Voss (2002), Calibration of Sun photometers and sky radiance sensors, in *Ocean Optics Protocols for Satellite Ocean Color Sensor Validation, Revision 3*, edited by L. Mueller and G. S. Fargion, *NASA Tech. Memo., TM-20021-210004*, vol. 1, 76–90.

Rajeev, K., V. Ramanathan, and J. Meywerk (2000), Regional aerosol distribution and its long-range transport over the Indian Ocean, *J. Geophys. Res.*, *105*, 2029–2043.

Ramanathan, V., et al. (2001), Indian Ocean Experiment: An integrated analysis of the climate forcing and effects of the great Indo-Asian haze, *J. Geophys. Res.*, *106*, 28,371–28,398.

Rasch, P. J., et al. (2000), A comparison of scavenging and deposition processes in global models: Results from the WCRP Cambridge Workshop of 1995, *Tellus, Ser. B*, *52*, 1025–1056, doi:10.1034/j.1600-0889.2000.00980.x.

Rasch, P. J., W. D. Collins, and B. E. Eaton (2001), Understanding the Indian Ocean Experiment (INDOEX) aerosol distributions with an aerosol assimilation, *J. Geophys. Res.*, *106*, 7337–7355.

Rogers, C. F., J. G. Hudson, B. Zielinska, R. L. Tanner, J. Hallett, and J. G. Watson (1991), Cloud condensation nuclei from biomass burning, in *Global Biomass Burning: Atmospheric, Climatic, and Biospheric Implications*, edited by J. S. Levine, pp. 431–438, MIT Press, Cambridge, Mass.

Rosen, J., S. Young, J. Laby, N. Kjorne, and J. Gras (2000), Springtime aerosol layers in the free troposphere over Australia: Mildura Aerosol Tropospheric Experiment (MATE 98), *J. Geophys. Res.*, *105*, 17,833–17,842.

Royer, P., P. Chazette, M. Lardier, and L. Sauvage (2011), Aerosol content survey by mini N_2-Raman lidar: Application to local and long-range transport aerosols, *Atmos. Environ.*, doi:10.1016/j.atmosenv.2010.11.001, in press.

Russell, L. M., D. H. Lenschow, K. K. Laursen, P. B. Krummel, S. T. Siems, A. R. Bandy, D. C. Thornton, and T. S. Bate (1998), Bidirectional mixing in an ACE 1 marine boundary layer overlain by a second turbulent layer, *J. Geophys. Res.*, *103*, 16,411–16,432.

Smirnov, A., Y. Villevalde, N. T. O'Neill, A. Royer, and A. Tarussov (1995), Aerosol optical depth over the oceans: Analysis in terms of synoptic air mass types, *J. Geophys. Res.*, *100*, 16,639–16,650.

Smirnov, A., B. N. Holben, T. F. Eck, O. Dubovik, and I. Slutsker (2000), Cloud screening and quality control algorithms for the AERONET database, *Remote Sens. Environ.*, *73*, 337–349, doi:10.1016/S0034-4257(00)00109-7.

Smirnov, A., et al. (2009), Maritime Aerosol Network as a component of Aerosol Robotic Network, *J. Geophys. Res.*, *114*, D06204, doi:10.1029/2008JD011257.

Stohl, A., et al. (2005), Technical note: The Lagrangian particle dispersion model FLEXPART version 6.2, *Atmos. Chem. Phys.*, *5*, 2461–2474, doi:10.5194/acp-5-2461-2005.

Tanré, D., Y. J. Kaufman, M. Herman, and S. Mattoo (1997), Remote sensing of aerosol properties over oceans using the MODIS/EOS spectral radiances, *J. Geophys. Res.*, 16,971–16,988, doi:10.1029/96JD03437.

Welton, E. J. , K. J. Voss, P. K. Quinn, P. J. Flatau, K. Markowicz, J. R. Campbell, J. D. Spinhirne, H. R. Gordon, and J. E. Johnson (2002), Measurements of aerosol vertical profiles and optical properties during INDOEX 1999 using micropulse lidars, *J. Geophys. Res.*, *107*(D19), 8019, doi:10.1029/2000JD000038.

J.-L. Baray, Y. Courcoux, R. Delmas, and V. Duflot, Laboratoire de l'Atmosphère et des Cyclones, Université de la Réunion, UMR CNRS-Météo-France 8105, Saint-Denis, Réunion F-97715, France. (vduflot@univ-reunion.fr)

P. Chazette and P. Royer, Laboratoire des Sciences du Climat et de l'Environnement, UMR CEA-CNRS-UVSQ 8212, Gif-sur-Yvette F-91191, France.